

MINISTRY OF EDUCATION AND TRAINING

QUY NHON UNIVERSITY

TRAN DOAN AN

**MODIFICATION OF $g\text{-C}_3\text{N}_4$ MATERIAL WITH NON-METALLIC
ELEMENTS AS PHOTOCATALYSTS UNDER VISIBLE-LIGHT**

Major : Theoretical and Physical Chemistry

Code : 9 44 01 19

PhD THESIS IN CHEMISTRY

BINH DINH, 2021

The study is carried out at
University of Education, Quy Nhon University

Supervisors: Assoc. Prof. VO VIEN
 Assoc. Prof. NGUYEN PHI HUNG

Reviewer 1: Prof. DUONG TUAN QUANG

Reviewer 2: Assoc. Prof. NGUYEN THI DIEU CAM

Reviewer 3: Dr. TRUONG MINH TRI

The thesis was assessed by University Examination Board at Quy Nhon University, An Duong
Vuong Str. 170, Quy Nhon city, Binh Dinh Province.

At,, 2021.

The thesis can be found at:

- Library of Quy Nhon University
- Vietnam National Library (31 Trang Thi Str., Hoan kien, Ha noi)

I. INTRODUCTION

1. Thesis statement

Photocatalysis research is attracting worldwide attention. Usually, photocatalysts are oxide or salt semiconductors such as TiO_2 , ZnO , MoS_2 , CdS or Ag_3PO_4 . Recently, graphite carbon nitride ($\text{g-C}_3\text{N}_4$) has emerged as a novel photocatalyst to split water into hydrogen, reducing CO_2 and degrade pollutants in the visible light region. This material shows higher photocatalytic efficiency in the visible light region than the traditional photocatalyst TiO_2 . However, $\text{g-C}_3\text{N}_4$ still exhibits unsatisfactory photocatalytic performance due to limitations such as fast photogenerated electron and hole recombination rate, low charge transfer capacity, and small specific surface area, high surface inertness, poor visible absorption, slow reaction kinetics, medium oxidation capacity, low charge carrier mobility.

In order to increase the photocatalytic efficiency of $\text{g-C}_3\text{N}_4$ materials, many different modification techniques have been implemented such as doping, nanostructure preparation, surface modification, grafting with semiconductor materials such as TiO_2 , WO_3 , Cu_2O , SnO_2 , ZnO , SnS_2 . Among them, the technique of doping halogen or O, S elements is attracting more and more attention of scientists around the world, because this technique can transform the band gap efficiently and simply.

Compared with metals, nonmetals have high ionization energy and electronegativity. Therefore, nonmetals can form covalent bonds with carbon and nitrogen atoms in the $\text{g-C}_3\text{N}_4$ lattice, leading to enhanced photocatalytic efficiency. This result is due to the enhancement of optical absorption, prolonging the lifetime of the photogenerated electron-hole, which helps to limit the recombination of the electron pair, while increasing the surface area. However, the number of published works on this doping is limited and only stops at doping each element, no rules have been found in the doping process and no research on O-F-co-doping has been found.

Based on the above analysis, we chose the topic “*Modification of $\text{g-C}_3\text{N}_4$ material with non-metallic elements as photocatalysts under the visible-light*” for the thesis.

2. The task of the thesis

Synthesis of materials $\text{g-C}_3\text{N}_4$ doped with halogen (VIIA group), chalcogen (VIA group) and co-doped two elements, then finding the best representatives for each group and the order for those in the same group.

3. Scope and object of the thesis

The research object of the thesis is as follows: The synthesis of g-C₃N₄ material doped with halogen (VII), chalcogen (VI) and co-doped two elements which are the two best representatives for groups VI and VII.

Research scope: Study on the preparation of F-doped g-C₃N₄ material, then find the optimal doping ratio. Based on this, other halogen elements are also investigated and do the comparison. This is followed by the study of individual O and S doping. Finally, a sample of co-doping of two elements (VI and VII groups) was addressed.

4. Scientific and practical meaning of the thesis

Scientific significance: Successfully synthesized g-C₃N₄ materials doped with elements F, Cl, Br, I, O, S and co-doped with two elements F and O by simple method. The relationship between the position in the periodic table of doped elements and their catalytic activity has been determined.

Practical significance: The obtained materials have very high practical application in the treatment of organic pollutants in wastewater.

5. Contributions of the thesis

- The new point of the thesis is the successful doping of some non-metallic elements of the halogen group (VII group) and chalcogen (VI group) and finding the relationship between the catalytic activity of the doped materials and the periodicity of the doping materials.

- For the first time successful co-doping of two elements F and O by simple calcination method.

- Proposed kinetics and photocatalytic mechanism on materials, determined the path of RhB decomposition. In addition, a photocatalytic mechanism is also proposed.

6. Thesis structure

The thesis consists of 164 pages, including Introduction: 3 pages; Chapter 1: Theoretical overview: 30 pages; Chapter 2: Research content and methods: 17 pages; Chapter 3: Research results and discussion: 93 pages; Conclusion and Suggestions: 1 page; papers related to the thesis: 3 pages; References: 18 pages including 131 foreign references.

II. CONTENT OF THE THESIS

Chapter 1. Theory overview

Briefly scientific information on g-C₃N₄ was reviewed, including synthesis methods, denaturation techniques, and applications. On that basis, it helps to design an appropriate experiment for the topic. The review shows that g-C₃N₄ modified by nonmetals is a potential direction. However, the number of published works on this doping is limited and only stops at element doping, no rules have been found in the doping process and no research works on O-F-co-doping have been reported. Therefore, we focus on the synthesis of halogen, chalcogen-doped and O-F-co-doped g-C₃N₄ materials.

Chapter 2. Objectives and methods

2.1. Materials synthesis: g-C₃N₄ (symbol **CNU-550-1**) was prepared by heating urea at 550 °C for 1 hour. The F-doped g-C₃N₄ sample was prepared by heating a mixture of urea with NH₄F (95:5, 93:7, 90:10 by mass) at 550 °C for 1 h, and denoted as **n:mFCN**. The X-doped g-C₃N₄ sample (X: Cl, Br, I) was synthesized as the n:mFCN preparation, except replacing NH₄F with NH₄X and only a ratio of 93:7, symbolized as **93:7XCN**. Oxygen-doped materials were synthesized by heating pretreated urea with 30% H₂O₂ (V = 20, 40, 60 mL/10g urea powder) at 550 °C for 1 h, symbol **x-OCN** (x = V). S-doped material was synthesized by heating a mixture of urea and thiourea (with the mass ratio x:y 85:15, 75:25, 50:50) at 550 °C for 1 hour, symbol **x:ySCN**. The F and O co-doped samples were prepared by heating urea treated with 30% H₂O₂ with NH₄F at 550 °C for 1 h, symbol **O-FCN**.

2.2. Material characterization: Characterization methods include X-ray diffraction (XRD); Infrared spectrum (FT-IR); X-ray photoelectron spectroscopy (XPS); Scanning electron microscopy (SEM) and transmission (TEM); Ultraviolet-visible diffuse reflectance spectrum (UV- Vis - DRS); Photoluminescence (PL) spectrum.

2.3. Evaluation of photocatalytic activity: The photocatalytic activity of the material was evaluated by the degradation of rhodamine B in water. In addition, HPLC liquid chromatography combined with ESI ionization mass spectrometry was used to detect intermediates in the photochemical degradation of RhB.

Chapter 3. Results and discussion

3.1. Fluorine doped g-C₃N₄ material

3.1.1. Material characteristics

As presented in the experimental section, to study F-doping, 3 samples of materials with different ratios of 95:5FCN, 93:7FCN and 90:10FCN were synthesized. These samples along with the CNU-550-1 have been featured by XRD, IR, SEM and especially XPS. The results demonstrate that the doped materials still remain the g-C₃N₄ structure (Figure 3.2). In addition, successful doping is also demonstrated by high resolution XRD spectrum (Figure 3.3) and especially, the XPS result of a typical 93:7FCN sample. Figure 3.5 (b), (d) shows the appearance of C-F bond in 93:7FCN from the XPS spectrum of C1s and F1s.

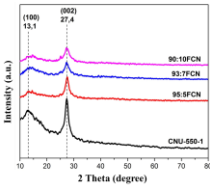


Figure 3.2. XRD patterns of CNU-550-1, 95:5FCN, 93:7FCN and 90:10FCN.

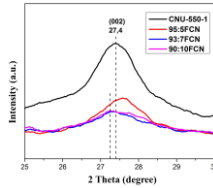


Figure 3.3. High-resolution XRD patterns of the CNU-550-1, 95:5FCN, 93:7FCN and 90:10FCN.

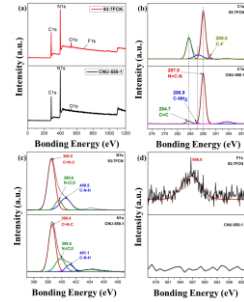


Figure 3.5. XPS (a) and high resolution XPS spectra of C1s (b), N 1s (c), F 1s (d) in CNU-550-1 and 93:7FCN

Figures 3.7 and 3.8 show that for the samples CNU-550-1, 95:5FCN, 93:7FCN and 90:10FCN, the absorption edge are redshifted from 451 to 456, 458 and 454 nm, corresponding to bandgap energy from 2.75; to 2.72; 2.71 and 2.73 eV, of which the 93:7FCN sample has the lowest band gap energy (2.71 eV).

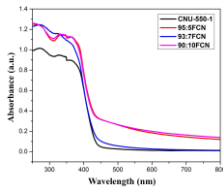


Figure 3.7. UV-Vis DRS spectra of CNU-550-1, 95:5FCN, 93:7FCN and 90:10FCN

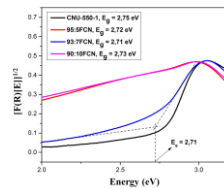


Figure 3.8. Kubelka–Munk function vs. the photon energy for the CNU-550-1, 95:5FCN, 93:7FCN and 90:10FCN

3.1.2. Investigation of photocatalytic activity

The photocatalytic activity (Figure 3.11) showed that the F-doped samples have higher degradation efficiency than pure g-C₃N₄, among which 93:7FCN exhibits the highest catalytic efficiency of 63.89 % after 140 minutes of lighting. Figure 3.12 confirms that 93:7FCN exhibits the highest photochemical reactivity with $k = 0.00695 \text{ min}^{-1}$. Therefore, this ratio was chosen to synthesize g-C₃N₄ materials doped with elements chlorine, bromine, iodine.

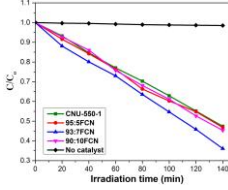


Figure 3.11. Graph showing the C/C_0 dependence over time of CNU-550-1, 95:5FCN, 93:7FCN and 90:10FCN

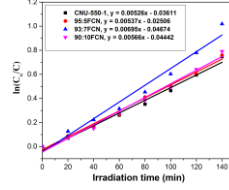


Figure 3.12. Langmuir – Hinshelwood kinetic models of CNU-550-1, 95:5FCN, 93:7FCN and 90:10FCN photocatalyst systems

3.2. g-C₃N₄ material doped with fluorine, chlorine, bromine and iodine

For comparison of halogen elements, in this section 93:7FCN material is also presented.

3.2.1. Material characteristics

- 3.2.1.1. *Material color*: All the doped materials have a darker yellow color than g-C₃N₄.
- 3.2.1.2. *X-ray diffraction pattern (XRD)*: Figure 3.14 and 3.15 shows that the halogen-doped g-C₃N₄ materials all have peaks characteristic for the structure of g-C₃N₄ and have a shift away from the peak at 27.4°, possibly due to the presence of elements F, Cl, Br and I in the g-C₃N₄ lattice.

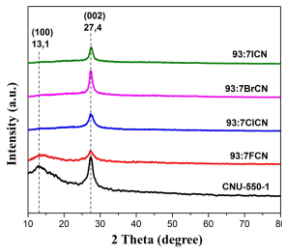


Figure 3.14. X-ray diffraction patterns of CNU-550-1, 93:7FCN, 93:7ClCN, 93:7BrCN and 93:7ICN samples

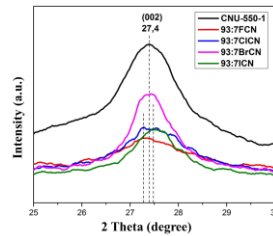


Figure 3.15. High-resolution X-ray diffraction patterns of CNU-550-1, 93:7FCN, 93:7ClCN, 93:7BrCN and 93:7ICN samples

- 3.2.1.3. *Infrared spectrum (IR)*: Infrared spectra are also characterized, showing that all doped samples have almost the same shape, which is characteristic of g-C₃N₄ material.

3.2.1.4. *X-ray photoelectron spectroscopy (XPS)*: Figure 3.19 shows the percentages of elements C, N, O, F, Cl, Br, I. In the composite samples, percentages of elements F, Cl, Br and I are 0.19%, 0.07%, 0.24% and 0.06%, respectively. Figure 3.20 shows the peak at 289.5 eV in sample 93:7FCN assigned to the $\text{Csp}^3\text{-F}$ bond; The peak at 288.5 eV for the samples 93:7ClCN and 93:7BrCN assigned to the C-(N)_3 group is the tertiary C in the aromatic rings, the Cl or Br atoms may have been settled in the adjacent layer of $\text{g-C}_3\text{N}_4$, which acts as a bridge between the nanosheets, for sample 93:7ICN the high peak at 285.2 eV proves C-I bonding, since I replaces N in the $\text{g-C}_3\text{N}_4$ lattice.

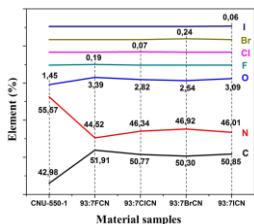


Figure 3.19. The graph shows the percentages of elements C, N, O, F, Cl, Br, I in CNU-550-1 and 93:7FCN, 93:7ClCN, 93:7BrCN, 93:7ICN samples

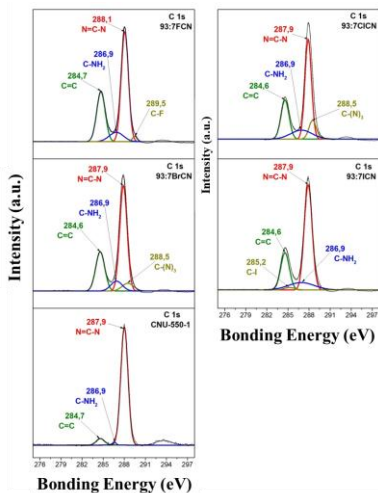


Figure 3.20. High-resolution XPS spectra of C 1s, in CNU-550-1 and 93:7FCN, 93:7ClCN, 93:7BrCN, 93:7ICN

Figure 3.22 shows that F 1s spectrum has peak at 686.6 eV of 93:7FCN sample representing C-F bond, Cl 2p spectrum is separated into 2 peaks at 197.5 and 199.7 eV corresponding to $\text{Cl } 2p^{3/2}$ and $\text{Cl } 2p^{1/2}$ for sample 93:7ClCN assigned to C-Cl bond group, Br 3d peak at 67.5 eV related to C-Br bond in 93:7BrCN sample and 2 I 3d peaks at 618.0 and 629.4 eV are assigned to $\text{C-I}3d^{5/2}$ and $\text{C-I}3d^{3/2}$ for 93:7ICN sample, the peak at 619.6 eV is thought to be the oxidation products of I during the reaction.

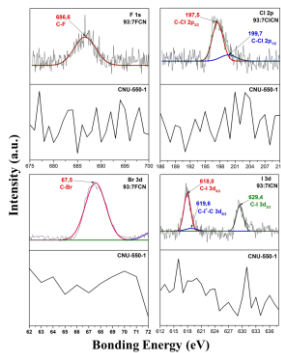


Figure 3.22. High resolution XPS spectra of F 1s, Cl 2p, Br 3d, I 3d in CNU-550-1 and 93:7FCN, 93:7ClCN, 93:7BrCN, 93:7ICN samples

3.2.1.5. *Scanning electron microscopy (SEM)*: SEM images show that the doped samples are not much different and are all characteristic for the structure of g-C₃N₄.

3.2.1.6. *Transmission electron microscopy (TEM)*: TEM images can detect halogen-doped g-C₃N₄ samples with the appearance of stacked 25 to 30 nm nanosheets.

3.2.1.7. *Ultraviolet-visible diffuse reflectance spectroscopy (UV-Vis DRS)*: The UV-Vis DRS spectra show that the absorption of the F, Cl, Br and I doped g-C₃N₄ samples exhibits a slight redshift up to 458, 456, 459 and 459 nm corresponding to Eg of 2.71, 2.72; 2.70 and 2.68 eV.

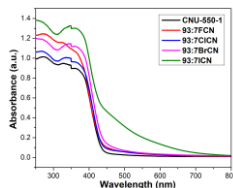


Figure 3.25. Solid-state UV-Vis spectra of CNU-550-1 and 93:7FCN, 93:7ClCN, 93:7BrCN, 93:7ICN samples

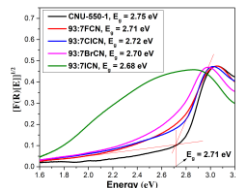


Figure 3.26. The Kubelka–Munk function vs. the photon energy of CNU-550-1 and F, Cl, Br, I doped g-C₃N₄ samples

3.2.1.8. *Fluorescence spectrum (PL)*: The PL emission peak intensity of the samples decreased in the order of 93:7ClCN > 93:7FCN > 93:7BrCN > CNU-550-1 > 93:7ICN. Peak intensity PL does not follow the rules in the periodic table. This is explained by the fact that the PL spectrum is also sensitive to exciton structure energy levels, impurities and crystal quality.

3.2.2. Investigation of photocatalytic activity

3.2.2.1. *Determining the time to reach adsorption equilibrium*: The samples of g-C₃N₄ doped with F, Cl, Br, I all reached adsorption equilibrium with RhB solution after about 2 hours.

3.2.2.2. *Investigation of photocatalytic activity of the materials:* Figure 3.31 shows that RhB decomposition on catalysts decreases in the order: 93:7FCN > 93:7ClCN > 93:7BrCN > 93:7ICN > CNU-550-1.

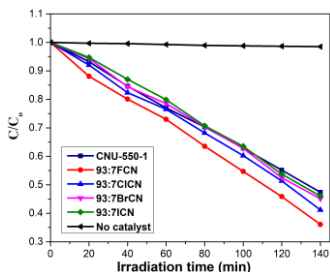


Figure 3.31. C/C_0 with time on CNU-550-1, 93:7FCN, 93:7ClCN, 93:7BrCN and 93:7ICN samples

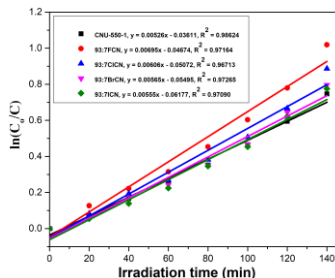


Figure 3.32. Langmuir - Hinshelwood kinetic model of the CNU-550-1, 93:7FCN, 93:7ClCN, 93:7BrCN and 93:7ICN photocatalyst

3.2.2.3. *Evaluation of the kinetics of the photocatalysis process:* Figure 3.32 shows that the photodegradation of RhB on the catalysts follows the Langmuir – Hinshelwood kinetic model, the rate constant k for the best sample 93:7FCN is 0.00695 min^{-1} , fold 1.15; 1.23; 1.25 and 1.32 times than that of the samples 93:7ClCN, 93:7BrCN, 93:7ICN and CNU-550-1, respectively. Interestingly, the photocatalytic activity follows the order: $F > Cl > Br > I$.

3.3. OXYGEN DOPED g- C_3N_4 MATERIAL

3.3.1. Material characteristics

3.3.1.1. *Material color:* All doped materials have a darker yellow color than g- C_3N_4 .

3.3.1.2. *X-ray diffraction pattern (XRD):* Figure 3.35 shows that all samples have peaks characteristic for the structure of g- C_3N_4 at 27.4° and 13.1° . Figure 3.36 shows that O-doped g- C_3N_4 has a decrease in peak intensity and a slight shift from 27.4° to 27.5° , related to the reduction of g- C_3N_4 layer distance from 0.325 nm to 0.322 nm.

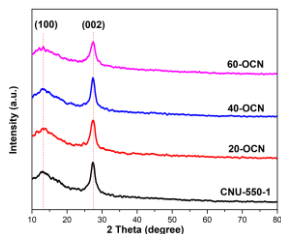


Figure 3.35. X-ray diffraction patterns of CNU-550-1, 20-OCN, 40-OCN and 60-OCN samples

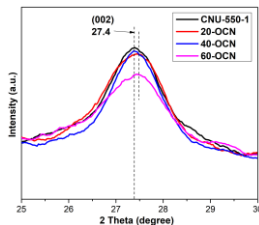


Figure 3.36. High-resolution XRD patterns in the (002) region of the CNU-550-1, 20-OCN, 40-OCN and 60-OCN samples

3.3.1.3. Infrared spectrum (IR): Figure 3.37 shows that the IR spectra of the O-doped g-C₃N₄ samples also have the same form as the IR spectrum of g-C₃N₄. However, the new peaks in the regions of 1200-1410 cm⁻¹ and 975-1150 cm⁻¹ can originate from fluctuations of the C-O bond in the C-O-C group. Thus, the peaks of O-containing groups in O-doped g-C₃N₄ may belong to the C-N(-C)-C trigonal region or the C-NH-C bridge. Therefore, the IR spectrum in this region has been considered in Figure 3.38.

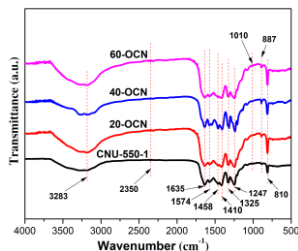


Figure 3.37. Infrared (IR) spectra of CNU-550-1, 20-OCN, 40-OCN and 60-OCN samples

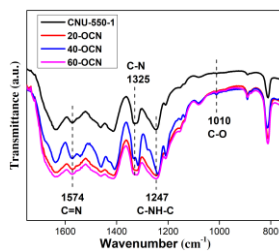


Figure 3.38. High-resolution IR spectra of CNU-550-1, 20-OCN, 40-OCN and 60-OCN samples

The 40-OCN sample appeared a new peak at 1010 cm⁻¹ that was assigned to the oscillation of C-O in the C-O-C group, and there was an additional high intensity peak near the peaks of 1574 and 1325. This proves that O may have been doped in g-C₃N₄ network.

3.3.1.4. X-ray photoelectron spectroscopy (XPS): Figure 3.40 shows that the percentage of O element in the O-doped g-C₃N₄ reached a maximum of 2.7% O in the 40-OCN sample, the %N in the 40-OCN sample decreased and %C increase compared to CNU-550-1 sample, it is possible that N is replaced by O and forms carbon graphite groups.

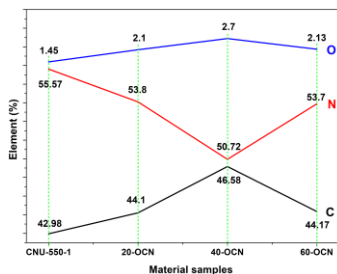


Figure 3.40. The graph depicts the percentages of elements C, N, and O in samples CNU-550-1, 20-OCN, 40-OCN and 60-OCN

In Figure 3.41, C 1s high-resolution XPS spectrum of O-doped g-C₃N₄ appeared peaks similar to g-C₃N₄. In addition, a new peak at 288.9 eV appears, representing the C-O bond. The 40-OCN sample shows an increase in Csp² peak intensity in C=C graphite

carbon group and decrease in Csp^2 peak intensity in N-C=N group compared with $\text{g-C}_3\text{N}_4$ sample.

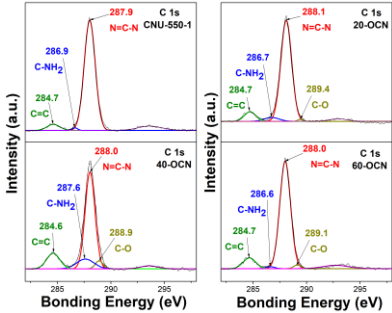


Figure 3.41. High-resolution XPS spectra of C 1s in CNU-550-1, 20-OCN, 40-OCN and 60-OCN samples

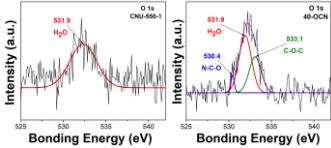


Figure 3.42. High-resolution XPS spectrum of O 1s in CNU-550-1 and 40-OCN

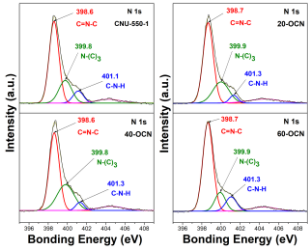


Figure 3.43. High-resolution XPS spectrum of N 1s in CNU-550-1, 20-OCN, 40-OCN and 60-OCN samples

Table 3.11. Value (%) of C-O peak area in CNU-550-1, 20-OCN, 40-OCN and 60-OCN samples

Peak area %	CNU-550-1	20-OCN	40-OCN	60-OCN
C-O	0	0.78	4.18	1.90

Table 3.11 shows that the C-O peak intensity is ranked in the order of 40-OCN > 60-OCN > 20-OCN, showing that 40-OCN has the highest concentration of doped oxygen in the $\text{g-C}_3\text{N}_4$ lattice. Figure 3.42 shows CNU-550-1 appearing only a single peak at 532.3 eV, assigned to the O^{2-} of the adsorbed water and no other peaks related to C-O or N-O binding. For 40-OCN, there are three peaks at 530.4; 531.9 and 533.1 eV, attributed to the oxygen forms in the N-C-O, adsorbed H_2O and C-O-C groups, respectively. This shows that O successfully doped into the $\text{g-C}_3\text{N}_4$ network. Figure 3.43 shows that O-doped $\text{g-C}_3\text{N}_4$ all appear similar peaks to $\text{g-C}_3\text{N}_4$. The value (%) of peak area and ratio C/N in the high-resolution XPS spectrum of N 1s are also determined in Table 3.12 and Table 3.13.

Table 3.12. Value (%) of peak area in the high-resolution XPS spectrum of N 1s

Sample \ Peak area %	C=N-C (Nsp ²)	Nsp ³		Regression coefficient R ²
		N-(C) ₃	C-N-H	
CNU-550-1	60.877	22.325	9.672	0.99813
20-OCN	60.505	25.216	9.553	0.99823
40-OCN	55.662	31.895	4.978	0.99819
60-OCN	66.145	14.447	11.475	0.99860

Table 3.13. C/N ratio and peak area percentage in the high-resolution XPS spectrum of N 1s in the CNU-550-1, 20-OCN, 40-OCN and 60-OCN samples

	CNU-550-1	20-OCN	40-OCN	60-OCN
C/N	0.774	0.819	0.914	0.823
Nsp ² /Nsp ³	1.903	1.740	1.509	2.552

High-resolution XPS spectra of C 1s, N 1s and O 1s of CNU-550-1, 20-OCN, 40-OCN and 60-OCN samples show an increase in C/N atomic ratio from 0.774 of CNU-550-1 to 0.819; 0.914 in 20-OCN; 40-OCN and the Nsp²/Nsp³ intensity ratio decreased from 1.903 of CNU-550-1 to 1.740; 1.509 of 20-OCN and 40-OCN. The above data confirmed that a small amount of N sp² atom in the g-C₃N₄ lattice of 20-OCN and 40-OCN was replaced by O, leading to the formation of C-O-C and N-C-O bonds.

The results of XPS analysis in 60-OCN also confirmed the formation of C-O bonds and increased C/N elemental ratio, but the Nsp²/Nsp³ ratio increased compared to CNU-550-1. In addition, the percentage of C-N-H peak area in Table 3.12 varies with the trend of 40-OCN < g-C₃N₄ ≈ 20-OCN < 60-OCN. Also, % peak N-(C)₃ obeys the order: 40-OCN > 20-OCN > g-C₃N₄ > 60-OCN. These data show that the condensation process is highly efficient with sample 40-OCN.

3.3.1.5. Scanning electron microscopy (SEM)

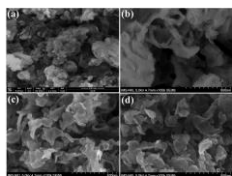


Figure 3.44. SEM images of CNU-550-1 (a), 20-OCN (b), 40-OCN (c) and 60-OCN (d)

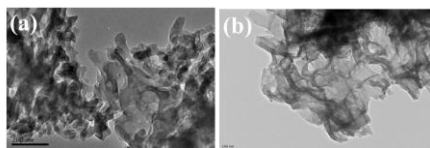


Figure 3.45. TEM images of CNU-550-1(a), 40-OCN(b)

SEM results (Figure 3.44) show that the O-doped g-C₃N₄ samples have a thin flake form of 25 to 30 nm, smooth winding and less tightly arranged than the bulk structure in CNU-550-1.

3.3.1.6. Transmission electron microscopy (TEM): Observing the TEM image at 100 nm scale (Figure 3.45), the appearance of thin, winding, stacked nanosheets with many 30 nm pores was obtained.

3.3.1.7. Ultraviolet-visible diffuse reflectance spectroscopy (UV-Vis DRS): Figure 3.46 shows that all O-doped samples have stronger absorption bands and shift to longer wavelength region.

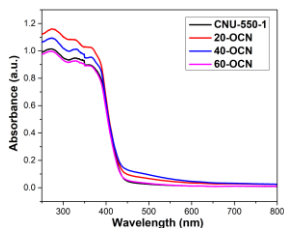


Figure 3.46. UV-Vis DRS spectra of CNU-550-1, 20-OCN, 40-OCN and 60-OCN samples

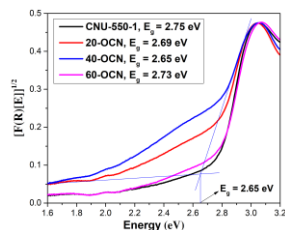


Figure 3.47. Bandgap of CNU-550-1, 20-OCN, 40-OCN and 60-OCN samples

In Figure 3.47, for g-C₃N₄ and 40-OCN, it is shown that the absorption edge is redshifted from 451 nm in CNU-550-1 to 468 nm for 40-OCN, corresponding to the band energy 2.75 eV and 2.65 eV.

3.3.1.8. Fluorescence Spectroscopy (PL): In Figure 3.48, the intensity of the PL emission peaks of the O-doped g-C₃N₄ samples were all reduced compared with that of the undoped g-C₃N₄ samples in the order: CNU-550-1 > 60-OCN > 20-OCN > 40-OCN. Among them, the photogenerated electron-hole recombination rate in the 40-OCN sample is the lowest.

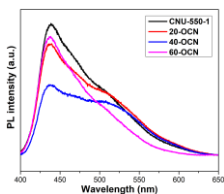


Figure 3.48. PL spectra of CNU-550-1, 20-OCN, 40-OCN and 60-OCN

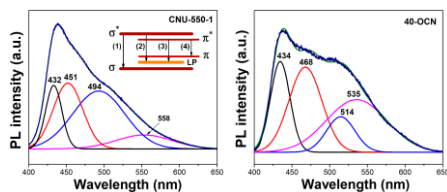


Figure 3.49. Deconvolution of PL spectra CNU-550-1 and 40-OCN

The PL spectra of CNU-550-1 and 40-OCN are separated into four symmetrical gaussian peaks and are presented in Figure 3.49 and Table 3.15.

Table 3.15. The wavelength and energy of the emission peaks were extracted from the PL spectra of CNU-550-1 and 40-OCN samples.

Sample	Emission peak							
	(1)		(2)		(3)		(4)	
	λ (nm)	E (eV)	λ (nm)	E (eV)	λ (nm)	E (eV)	λ (nm)	E (eV)
CNU-550-1	432	2.87	451	2.75	494	2.51	558	2.22
40-OCN	434	2.86	468	2.65	514	2.41	535	2.32

Figure 3.49 and Table 3.15 show that the O doping into g-C₃N₄ led to a change in the electronic structure of g-C₃N₄. In addition, the red shift at peak (2) to 468 nm for 40-OCN is consistent with the reduction of E_g in the UV-Vis DRS spectra. The four peaks from lower to higher wavelength correspond to the electronic transition (1) from conduction band σ^* to valence band σ , (2) from σ^* to LP, (3) from π^* to LP, and (4) from π^* to π , respectively. Figure 3.49 and Table 3.15 show a red shift of the first three peaks of 40-OCN relative to CNU-550-1. In contrast, a blue shift of the fourth peak is observed for 40-OCN relative to CNU-550-1, which is attributed the energy gap between the π and π^* bands of 40-OCN larger than that of the CNU-550-1.

3.3.2. Investigation of photocatalytic activity

3.3.2.1. Determining the time to reach adsorption equilibrium: The rhodamine B equilibrium adsorption time on CNU-550-1, 20-OCN, 40-OCN and 60-OCN is 2 hours.

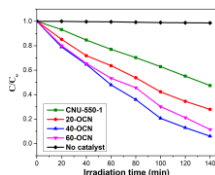


Figure 3.51. C/C_0 vs. time for CNU-550-1, 20-OCN, 40-OCN and 60-OCN

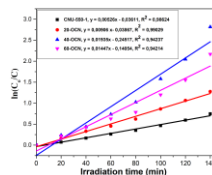


Figure 3.52. Langmuir – Hinshelwood kinetic models of CNU-550-1, 20-OCN, 40-OCN and 60-OCN

3.3.2.2. Investigation of photocatalytic activity of materials: Figure 3.51 shows that the degradation efficiency of RhB in water of the samples increases in the order: CNU-550-1 < 20-OCN < 60-OCN < 40-OCN. After 140 minutes, 40-OCN showed the highest RhB degradation efficiency of 94.03 %, 1.77 times higher than that of CNU-550-1.

3.3.2.3. Kinetic evaluation of photocatalysis: Figure 3.52 confirms that 40-OCN has the highest reaction rate constant of 0.01935 min⁻¹, which is 3.68, 2.14; 1.33 times higher than that of CNU-550-1, 20-OCN, 60-OCN, respectively.

The ability to maintain the catalytic activity of 40-OCN is shown in *Figure 3.53*, showing that after 5 times of photocatalysis, the photocatalytic activity of the composite decreased by 8.1%.

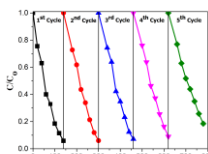


Figure 3.53. Change of RhB concentration with reaction time of 40-OCN sample after 5 cycles

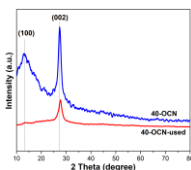


Figure 3.54. X-ray diffraction pattern of 40-OCN and 40-OCN-used

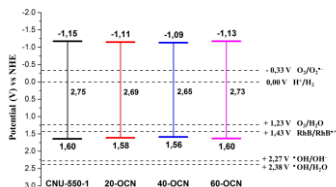


Figure 3.55. Power levels of CNU-550-1, 20-OCN, 40-OCN and 60-OCN

The structure of 40-OCN after 5 cycles was characterized by XRD (*Figure 3.54*), showing that the order of the inner surface of the triazine ring (100 plane) decreased, while the order of adjacent layers was intercalated. Interstitial of the graphitic structure (002 plane) was almost unchanged in this sample compared with 40-OCN. The photocatalytic degradation mechanism of the material samples was studied through analysis of valence band (E_{VB}) and conduction band (E_{CB}) potential. *Figure 3.55* shows that, for O-doping, the potential E_{VB} decreases and the E_{CB} increases. From the band gap energy analysis results, we found that the $O_2^{\bullet -}$ active group plays a key role in the photocatalysis of RhB degradation. Experiments to investigate the influence of $O_2^{\bullet -}$, $\cdot OH$, h^+ , e^- groups were also conducted. With the addition of quenchers for RhB degradation such as 1,4-benzoquinone (1,4-BQ), tert-butyl alcohol (TBA), disodium ethylenediaminetetraacetate (2Na-EDTA), dimethyl sulfoxide (DMSO)) is the quenching agent of the corresponding active groups $O_2^{\bullet -}$, $\cdot OH$, h^+ , e^- .

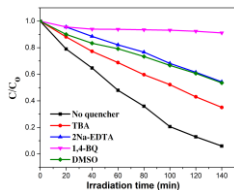


Figure 3.56. Effect of quenching agent on RhB degradation in 40-OCN sample.

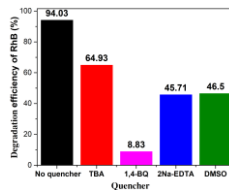


Figure 3.57. Decomposition efficiency of RhB in the presence of quenching agent.

Figure 3.56 and *Figure 3.57* show that the photocatalytic efficiency of RhB was reduced in the presence of quenching agent and the role of active agents in photocatalysis in the order: $O_2^{\bullet -} > h^+ \approx e^- > \cdot OH$. This result is completely consistent with the proposed mechanism through potential energy analysis presented in *Figure 3.55*.

To investigate RhB degradation, HPLC combined with ESI ionization mass spectrometry was used to detect intermediates. The obtained m/z values of the intermediates were 399, 355, 311, 327, 282 (*Figure 3.59*). It is worth noting that in the study of this thesis, the oxidation of N-dealkyl and C-C cleavage can also occur and the free radical $O_2^{\bullet-}$ can play an important role in the degradation of RhB.

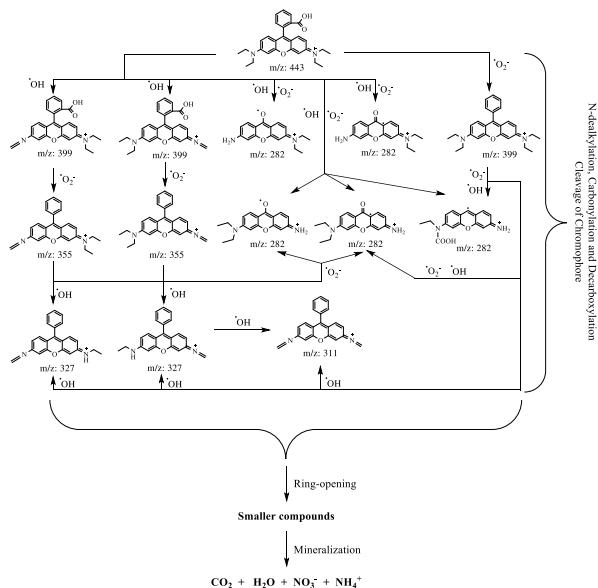
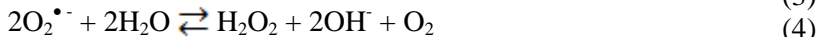


Figure 3.59. Proposed mechanism for the photodegradation of RhB.

Based on the UV-Vis DRS spectrum and the results of the trapping experiments, the mechanism of the photochemical degradation reaction of RhB in water through the oxygen-doped $g-C_3N_4$ system was proposed, as shown in *Figure 3.60*.



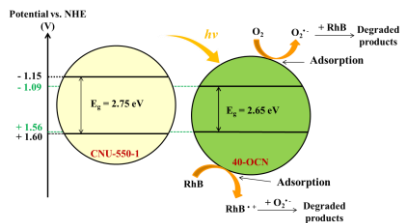


Figure 3.60. Proposed mechanism for photocatalytic degradation of RhB on x-OCN.

3.4. SULFUR DOPED g-C₃N₄ MATERIAL

3.4.1. Material characteristics

3.4.1.1. *Material color*: Compared to CNU-550-1, the yellow color of sulfur-doped g-C₃N₄ is darker.

3.4.1.2. *X-ray diffraction pattern (XRD)*: Figure 3.62 shows all sulfur-doped g-C₃N₄ obtained with two peaks at 27.4° and 13.4°, corresponding to the (002) and (100) planes. The XRD results indicate that the S-doped g-C₃N₄ leads to the structure of g-C₃N₄ which is indeed tilted, deformed and bent. The average crystal sizes for samples CNU-550-1, 85:15SCN, 75:25SCN and 50:50FCN are 2.53; 2.12; 2.32 and 3.07 nm, respectively.

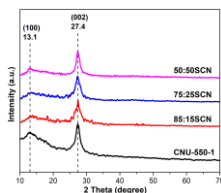


Figure 3.62. XRD patterns of CNU-550-1, 85:15SCN, 75:25SCN and 50:50SCN

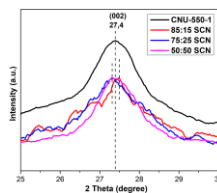


Figure 3.63. High-resolution XRD patterns of CNU-550-1, 85:15SCN, 75:25SCN and 50:50SCN

3.4.1.3. *Infrared spectrum (IR)*: Figure 3.64 shows the same shape for all samples, C-S vibrations at 1079 cm⁻¹ may be overlapped with C-N vibration in the 1200 - 1050 cm⁻¹ region.

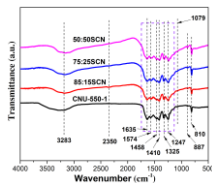


Figure 3.64. IR spectra of CNU-550-1, 85:15SCN, 75:25SCN and 50:50SCN

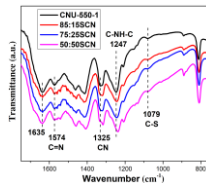


Figure 3.65. The resolved IR spectra of CNU-550-1, 85:15SCN, 75:25SCN and 50:50SCN

The S-doped g-C₃N₄ has a slight frequency shift of the peak at 1247 cm⁻¹ to 1240 cm⁻¹ and appears peaks from 1247 to 1574 cm⁻¹ compared with pure g-C₃N₄ as shown in *Figure 3.65*.

3.4.1.4. *The X-ray photoelectron spectroscopy (XPS) of the samples in Figure 3.66 (a) shows the presence of chemical elements O 1s, N 1s, C 1s on the surface of all material and S 2p for the S-doped g-C₃N₄ sample.*

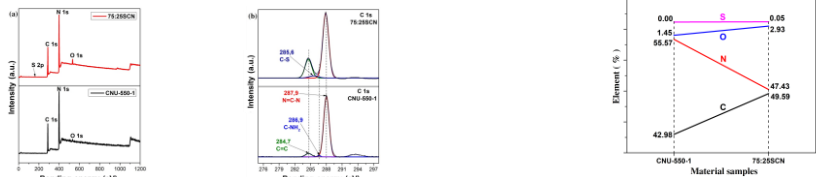


Figure 3.67. Graph depicting the percentages of C, N, O, and S elements in CNU-550-1 and 75:25SCN

Figure 3.66. XPS (a) and high-resolution XPS spectra of C 1s (b), N 1s (c), S 2p (d) in CNU-550-1 and 75:25SCN

The XPS spectrum of a representative sample 75:25SCN in *Figure 3.66 (b-d)* shows the appearance of C-S bonding in 75:25SCN from the XPS spectrum of C 1s and S 2p. In the S 2p XPS spectrum (*Figure 3.66 (d)*), the peak at 168.2 eV is attributed to the S=O of the intermediate product (SO₃²⁻ or SO₄²⁻) generated during thermal decomposition. The S 2p peak at 163.9 eV is assigned to the C-S links. The % value of peak area and ratio C/N, percentage of peak area in high resolution XPS spectrum of N 1s are also determined in *Table 3.21* and *Table 3.22*.

Table 3.21. Value (%) of peak area in the high-resolution XPS spectrum of N 1s

Sample \ Peak area %	C=N-C (Nsp ²)	Nsp ³		Regression coefficient R ²
		N-(C) ₃	C-N-H	
CNU-550-1	60.877	22.325	9.672	0.99813
75:25SCN	64.406	10.548	12.886	0.99845

Bảng 3.22. C/N ratios and peak area (%) in XPS spectrum of N 1s in CNU-550-1 and 75:25SCN

	CNU-550-1	75:25SCN
C/N	0.774	1.046
Nsp ² /Nsp ³	1.903	2.748

Table 3.21 and Table 3.22 show that the atomic C/N ratio increased from 0.774 in the CNU-550-1 to 1.046 for 75:25SCN and the Nsp^2/Nsp^3 intensity ratio increased from 1.903 in CNU-550-1 to 2.748, indicating that the doping of S elements into the $g-C_3N_4$ lattice can reduce N defect in the $-NH_2$ or $-NH$ groups.

3.4.1.5. *Scanning electron microscopy (SEM)* shows that the S-doped $g-C_3N_4$ sample had a smaller nanosheet structure with many slits and high porosity.

3.4.1.6. *Transmission electron microscopy (TEM)* shows the appearance of stacked nanosheets and many pores ~ 30 nm.

3.4.1.7. *Ultraviolet-visible diffuse reflectance spectroscopy (UV-Vis DRS)*: Figure 3.70 shows that the absorption band of all the S-doped samples is stronger and shifts to longer wavelength region with increasing weight of thiourea in the precursor mixtures.

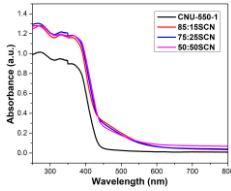


Figure 3.70. UV-Vis-DRS spectra of CNU-550-1 and S-doped $g-C_3N_4$.

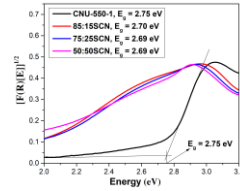


Figure 3.71. Kubelka–Munk function vs. the photon energy of CNU-550-1 and S-doped $g-C_3N_4$.

Figure 3.71 shows that the adsorption edge is red-shifted with a lower binding energy of 2.68 eV for S-doped $g-C_3N_4$ compared to 2.75 eV for the undoped sample, demonstrating a significant boost to the optical absorption efficiency.

3.4.1.8. *Fluorescence spectrum (PL)*: The PL intensity is in the order of CNU-550-1 > 75:25SCN (Figure 3.72).

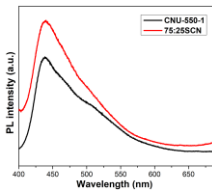


Figure 3.72. PL spectra of CNU-550-1 and 75:25SCN

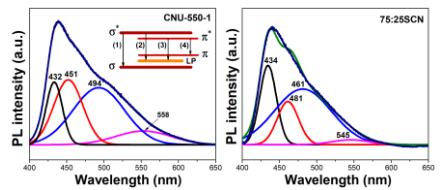


Figure 3.73. Deconvoluted PL spectra of CNU-550-1 and 75:25SCN

Figure 3.73 and Table 3.24 show that S-doping into $g-C_3N_4$ led to a change in the electronic structure of $g-C_3N_4$. The red shift at peak (2) is related to the $\sigma^* - LP$ transition from 451 nm of $g-C_3N_4$ (2.75 eV) to 461 nm (2.69 eV) for 75:25SCN in accordance with

UV-Vis DRS characteristics. The electronic band state model of g-C₃N₄ was presented in section 3.2.1.8, Figure 3.29 explained these emission peaks (1), (2), (3) and (4).

3.4.2. Investigation of photocatalytic activity

3.4.2.1. Determination of time to reach adsorption equilibrium: The results show that CNU-550-1 and S-doped g-C₃N₄ both reached adsorption equilibrium with RhB solution after about 2 hours.

3.4.2.2. Investigation of the photocatalytic activity of the material: Figure 3.75 shows that 75:25SCN exhibits the highest conversion of 91.96%, 1.75 times higher than that of pure g-C₃N₄, while 85:15SCN and 50:50SCN have efficiencies of 79.40 % and 55.02 %, respectively, after 140 minutes of visible light irradiation.

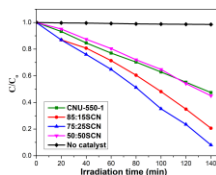


Figure 3.75. C/C_0 vs. time for CNU 550-1, 85:15SCN, 75:25SCN and 50:50SCN

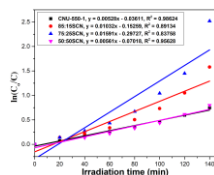


Figure 3.76. Langmuir – Hinshelwood kinetic models of CNU-550-1 and 85:15SCN, 75:25SCN, 50:50SCN

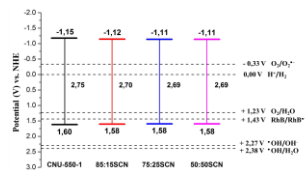


Figure 3.77. Energy levels of CNU-550-1, 85:15SCN, 75:25SCN and 50:50SCN

3.4.2.3. Kinetic evaluation of the photocatalysis process: In Figure 3.76, the kinetic results confirm that 75:25SCN has the highest k reaction rate constant of 0.01591 min^{-1} . The photochemical degradation mechanism is similarly proposed in Section 3.2.2.3. Figure 3.77 shows that the active group $\text{O}_2^{\cdot -}$ plays a key role in the photocatalysis of RhB degradation.

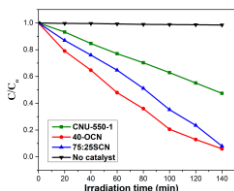


Figure 3.78. C/C_0 vs. irradiation time of CNU-550-1, 75:25SCN and 40-OCN.

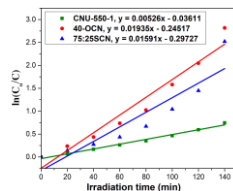


Figure 3.79. Langmuir - Hinshelwood kinetic models of CNU-550-1, 75:25SCN and 40-OCN.

Figure 3.78 and Figure 3.79 show that the RhB degradation efficiency and reaction rate constant of 40-OCN are 94.03 % and 0.01935 min^{-1} , respectively, are higher than that of 75:25SCN (91,96 % and 0.01591 min^{-1}). This shows that oxygen is the best candidate chosen to co-doped with fluorine into the g- C_3N_4 lattice to improve the defect of the fluorine-doped g- C_3N_4 photocatalyst (denoted as 93:7FCN).

3.5. OXYGEN AND FLUORINE CO-DOPED g- C_3N_4 MATERIAL

3.5.1. Material characteristics

3.5.1.1. Material color: The yellow color of the O-FCN is darker than that of CNU-550-1, 93:7FCN and 40-OCN.

3.5.1.2. X-ray diffraction pattern (XRD): Figure 3.81 shows all doped g- C_3N_4 products obtained with two peaks at 27.4° and 13.4° . However, with O-FCN (Figure 3.82), the 2θ position for the plane (002) increased to 27.8° ($d = 0.321 \text{ nm}$). Average crystal sizes of CNU-550-1, 93:7FCN, 40-OCN and O-FCN are 2.53; 1.13; 2.89 and 3.78 nm, respectively.

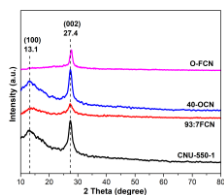


Figure 3.81. XRD patterns of CNU-550-1, 85:15SCN, 75:25SCN and 50:50SCN.

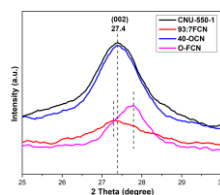


Figure 3.82. The expanded XRD patterns of CNU-550-1, 85:15SCN, 75:25SCN and 50:50SCN.

3.5.1.3. IR spectra: Figure 3.83 shows identical IR spectra for all samples. However, the O-F co-doped g- C_3N_4 reduced the peak intensity and increased the peak position at 1462 to 1574 cm^{-1} compared with pure g- C_3N_4 (Figure 3.84).

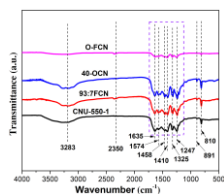


Figure 3.83. IR spectra of CNU-550-1, 93:7FCN, 40-OCN and O-FCN

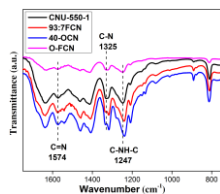


Figure 3.84. Expanded IR spectra of CNU-550-1, 93:7FCN, 40-OCN and O-FCN

3.5.1.4. X-ray photoelectron spectroscopy (XPS)

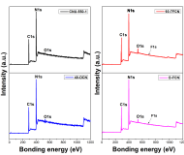


Figure 3.85. XPS spectra of CNU-550-1, 93:7FCN, 40-OCN and O-FCN.

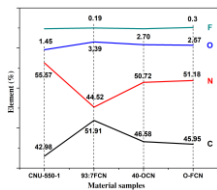


Figure 3.86. XPS spectra of CNU-550-1, 93:7FCN, 40-OCN and O-FCN.

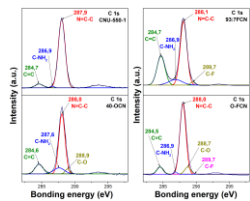


Figure 3.87. The high-resolution XPS spectra of C 1s in CNU-550-1, 93:7FCN, 40-OCN and O-FCN.

Figure 3.85 shows the presence of elements O 1s, N 1s, C 1s, F 1s on the surface of all the material samples with the percentage of elements shown in Figure 3.86. For O-FCN shown in Figure 3.87 and Figure 3.89, it shows that O-FCN appears C-F and C-O bonds, corresponding to the peak area of 0.12 and 8.28%, respectively, from the XPS spectra of C 1s, F 1s and O 1s. Figure 3.88 shows the N 1s high-resolution XPS spectrum of the samples.

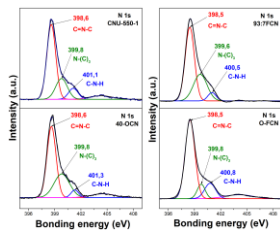


Figure 3.88. High-resolution XPS spectra of N 1s.

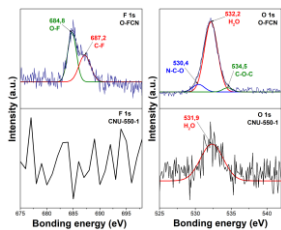


Figure 3.89. High-resolution spectra of F 1s, O 1s in CNU-550-1 and O-FCN.

The value (%) of peak area and ratio C/N in the high resolution XPS spectrum of N 1s are also determined in Table 3.28 and Table 3.29.

Table 3.28. Value (%) of peak area in the high-resolution XPS spectrum of N 1s.

Sample \ Peak area (%)	C=N-C (Nsp ²)	Nsp ³		Regression coefficient R ²
		N-(C) ₃	C-N-H	
CNU-550-1	60.877	22.325	9.672	0.99813
93:7FCN	61.117	32.722	6.161	0.99937
40-OCN	55.662	31.895	4.978	0.99819
O-FCN	66.175	9.930	14.562	0.99765

Table 3.29. C/N ratio and peak area % ratio in the high-resolution XPS spectra of N 1s in CNU-550-1, 93:7FCN, 40-OCN and O-FCN samples

	CNU-550-1	93:7FCN	40-OCN	O-FCN
C/N	0.774	1.166	0.914	0.898
Nsp²/Nsp³	1.903	1.572	1.509	2.702

Table 3.28 and Table 3.29 show that the atomic C/N ratio increases in the order: CNU-550-1 < O-FCN < 40-OCN < 93:7FCN and the Nsp²/Nsp³ intensity ratio of O-FCN is 2.702 times higher than that of other samples, indicating that the co-doping of F and O into the g-C₃N₄ lattice can reduce the N defect in the -NH₂ or -NH groups.

3.5.1.5. SEM data show that O-FCN possesses a thin nanosheet structure similar to those of 93:7FCN, 40-OCN.

3.5.1.6. TEM images show that O-FCN has the appearance of thin, bent, stacked nanosheets and many pores with diameter of ~ 30 nm.

3.5.1.7. UV-Vis DRS: Figure 3.92 shows that the absorption of all the samples 93:7FCN, 40-OCN and O-FCN shifts to the longer wavelength region. The band gap energies of the samples are shown in Figure 3.93.

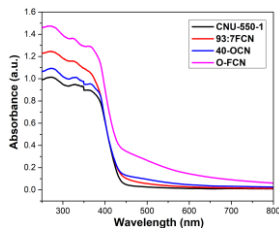


Figure 3.92. UV-Vis DRS spectra of CNU-550-1, 93:7FCN, 40-OCN and O-FCN

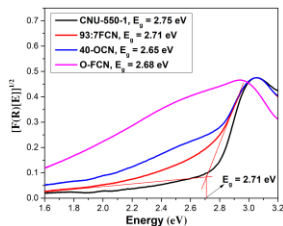


Figure 3.93. Kubelka–Munk function vs. photon energy for CNU-550-1, 93:7FCN, 40-OCN and O-FCN

Interestingly, when O, F co-doping into the g-C₃N₄ lattice, the absorption edge red-shifts with a wavelength of 463 nm (2.68 eV) compared to the average value of 93:7FCN (458 nm, 2.71 eV) and 40-OCN sample (463 nm, 2.65 eV), indicating that oxygen doping plays an important role in increasing the absorbance in the visible region of O-FCN compared to 93:7FCN.

3.5.1.8 . PL spectrum: Figure 3.94 shows that the luminescence intensity of O-FCN is lower than that of CNU-550-1 and decreases in the order of 93:7FCN > CNU-550-1 > O-FCN > 40-OCN.

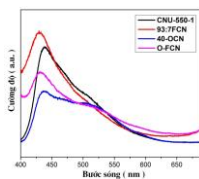


Figure 3.94. PL spectra of CNU-550-1, 93:7FCN, 40-OCN and O-FCN.

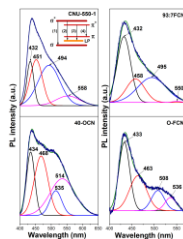


Figure 3.95. Deconvoluted PL spectra of CNU-550-1, 93:7FCN, 40-OCN and O-FCN.

The PL spectra of CNU-550-1 and the samples are deconvoluted into 4 symmetrical gaussian peaks and presented in *Figure 3.95*, shows that the deconvoluted PL spectra of O-FCN are similar to that of 93:7FCN, 40-OCN.

3.5.2. Investigation of photocatalytic activity

3.5.2.1. Determine the time to reach adsorption equilibrium: O-FCN, CNU-550-1, 93:7FCN and 40-OCN samples all reached adsorption equilibrium with RhB solution after about 2 hours.

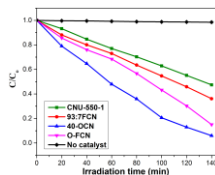


Figure 3.97. C/C_0 vs. irradiation time for CNU-550-1, 93:7FCN, 40-OCN and O-FCN.

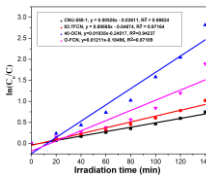


Figure 3.98. Langmuir – Hinshelwood kinetic model of CNU-550-1, 93:7FCN, 40-OCN and O-FCN.

3.5.2.2. Investigation of the photocatalytic activity of the material: *Figure 3.97* shows the RhB decomposition efficiency after 140 minutes under visible light irradiation for O-FCN of 84.96%, higher 1.33 and 1.62 times than 93:7FCN and CNU-550-1, respectively. The photocatalytic performance of the samples increased in the order of CNU-550-1 < 93:7FCN < O-FCN < 40-OCN.

3.5.2.3. Kinetic evaluation of the photocatalysis process: *Figure 3.98* shows that the rate constant k for the O-FCN sample is 1.83 and 2.42 times higher than that of 93:7FCN and CNU-550-1, respectively. The photochemical degradation mechanism has been similarly proposed in the section 3.2.2.3.

The co-doping of oxygen and fluorine into the $g\text{-C}_3\text{N}_4$ lattice created a synergic effect, improving the photocatalytic efficiency of the O-FCN material ($k = 0.01211 \text{ min}^{-1}$) higher than that of 93:7FCN ($k = 0.00695 \text{ min}^{-1}$). The research results in this thesis have

provided additional data to prove that the oxygen doping agent is the best and promising candidate for modifying g-C₃N₄ to improve the photocatalytic activity in visible light region.

CONCLUSIONS AND SUGGESTIONS

Conclusions

1. The g-C₃N₄ materials doped with F, Cl, Br and I by a simple calcination in solid phase of urea and NH₄X precursors (X = F, Cl, Br and I) were successfully synthesized. The doped materials have better RhB photocatalytic activity than the undoped samples and follows the order F > Cl > Br > I.

2. The materials g-C₃N₄ doped with O and S were successfully synthesized from the precursors of urea pretreated with H₂O₂ or thiourea, respectively, by a simple solid-phase calcination method. The doped materials exhibit better photodegradation of RhB than the undoped materials. Of the two elements, O-doped g-C₃N₄ performs the photocatalytic activity better than the S-doped one. Especially, among the O-doped samples, 40-OCN performs the best photocatalytic activity even compared with the halogen-doped materials.

3. The co-doped materials with two elements F and O were successfully synthesized. The photodegradation of RhB over the co-doped ones is not good as the O doping but better than the F doped one. However, this was a new observation in the co-doped synthesis .

4. Kinetics and photocatalysis mechanism were proposed for the prepared materials. Accordingly, all photodegradations followed the pseudo-first-order kinetics, the superoxide anion radical O₂^{•-} plays an important role and determines the path of RhB degradation. In addition, a photocatalytic mechanism is also proposed.

5. Doped materials have higher RhB decomposition efficiency than undoped materials and increase in the order of CNU-550-1 < 93:7ICN < 93:7BrCN < 93:7ClCN < 93:7FCN < O- FCN < 75:25SCN < 40-OCN, corresponding to RhB degradation percentage of 52.60 %, 53.96 %, 54.89%, 58.81%, 63.89%, 84.96%, 91 ,96 %, 94.03 %.

Suggestions

1. Photocatalytic ability to degrade other organic substances should also be studied to find how the organic-pollutant structures affect the photocatalytic activities of the materials.

2. The immobilization of catalysts on suitable substrates to transfer these materials from lab scale to practical applications.

PAPERS RELATED TO THE THESIS

1. **Tran Doan An**, Nguyen Van Phuc, Nguyen Phi Hung, Vo Vien (2017), "Effect of synthesis conditions on photocatalytic activity of g-C₃N₄", *Vietnam Journal of Catalysis and Adsorption*, vol. 6, No. 3/2017, p. 20-24.
2. Tran Huu Ha, **Tran Doan An**, Nguyen Van Phuc, Nguyen Thi Viet Nga, Truong Duy Huong, Nguyen Phi Hung, Vo Vien (2017), "Synthesis and modification of g-C₃N₄ with MS₂ (M = Mo, W) for photocatalyst application", *Quy Nhon University Journal of Science*, vol. 11, No. 5/2017, p 23-32
3. Nguyen Pham Chi Thanh, **Tran Doan An**, Nguyen Van Phuc, Nguyen Tan Lam, Ho Van Ban, Nguyen Phi Hung, Vo Vien (2019), "Study on synthesis of oxygen-doped g-C₃N₄ as a photocatalyst", *Vietnam Journal of Catalysis and Adsorption*, vol. 8, No. 3/2019, p. 32-37.
4. **An Tran Doan**, Phuc Nguyen Van, Tri Nguyen Ngoc, Phu Huynh Thi, Hung Nguyen Phi, and Vo Vien (2019), "Sulfur-doped g-C₃N₄ with enhanced visible-light photocatalytic activity", *Applied Mechanics and Materials*, Trans Tech Publ, vol.889, pp. 43-50.
5. Phuc Nguyen Van, **An Doan Tran**, Tri Nguyen Ngoc, Ha Tran Huu, Hien Tran Thi Thu, Hung Nguyen Phi, and Vo Vien (2019), "Synthesis and Photocatalytic Activity of Fluorine doped-g-C₃N₄", *Applied Mechanics and Materials*, Trans Tech Publ, vol.889, pp. 24-32.
6. **An Tran Doan**, Phuc Nguyen Van, Tri Nguyen Ngoc, Hung Nguyen Phi, Vien Vo (2017), "Effects of synthesis conditions on photocatalytic activity of g-C₃N₄", *Proceedings of The 6th Asian Symposium on Advanced Materials*, Hanoi, Vietnam, VO-2, pp. 87-92.
7. **Doan An Tran**, Chi Thanh Nguyen Pham, Tri Nguyen Ngoc, Hung Nguyen Phi, Qui Thanh Hoai Ta, Duy Huong Truong, Van Thang Nguyen, Huy Hoang Luc, Le Tuan Nguyen, Ngoc Nhiem Dao, Sung Jin Kim, Vien Vo (2021), "One-step synthesis of oxygen doped g-C₃N₄ for enhanced visible-light photodegradation of Rhodamine B", *Journal of Physics and Chemistry of Solids*, 151, 109900, <https://doi.org/10.1016/j.jpcs.2020.109900>